

Validation of statistical estimation of transmission loss in the presence of geoacoustic inversion uncertainty

Chen-Fen Huang, Peter Gerstoft, and William S. Hodgkiss

Marine Physical Laboratory, Scripps Institution of Oceanography, La Jolla, California 92093-0238

(Received 21 March 2006; revised 10 July 2006; accepted 10 July 2006)

Often the ocean acoustic environment is not well known and sonar performance prediction will be affected by this uncertainty. Here, a method for estimating transmission loss (TL) is proposed which incorporates these environmental uncertainties. Specifically, we derive an approach for the statistical estimation of TL based on the posterior probability density of environmental parameters obtained from the geoacoustic inversion process. First, a Markov chain Monte Carlo procedure is employed in the inversion process to sample the posterior probability density of the geoacoustic parameters. Then, these sampled parameters are mapped to the transmission loss domain where a full multidimensional probability distribution of TL as a function of range and depth is obtained. In addition, TL is also characterized by its summary statistics including the median, percentiles, and correlation coefficients. The approach is illustrated using a data set obtained from the ASIAEX 2001 East China Sea experiment. Based on the geoacoustic inversion results, the predicted TL and its variability are estimated and then compared with the measured TL. In general, there is a good agreement with the percentage of observed number of data points inside the credibility interval.

© 2006 Acoustical Society of America. [DOI: 10.1121/1.2261356]

PACS number(s): 43.30.Pc, 43.60.Pt [AIT]

Pages: 1932–1941

I. INTRODUCTION

Statistical estimation of geoacoustic parameters from acoustic field data has been an active research topic for more than a decade.^{1–7} This paper proposes to use the parameter uncertainties obtained during the geoacoustic inversion process to make a statistical estimation of transmission loss (TL). The transmission loss domain is important as it can be used in connection with sonar performance prediction (e.g., Ref. 8 and in particular the paper by Abbot and Dyer⁹).

Analytical approaches to transfer uncertainties have been adopted by several authors. Reference 10 derived an analytical expression for quantifying the uncertainty in predicted acoustic fields produced by environmental uncertainties. Reference 11 describes how uncertainty can be embedded into ocean acoustic propagation models through expansions of the input parameter uncertainties in orthogonal polynomials. The disadvantage of these approaches is that they are less flexible computationally and so far have only been used on simple problems.

Monte Carlo methods for sampling the environmental variability have been studied by several authors (e.g., Refs. 12 and 13). Random realizations of the acoustic environment are propagated via the deterministic wave equation to produce realizations of the acoustic field. Mean and higher moments are used to characterize the acoustic variability. While thousands of simulations generally are required, these computations are fast, simple, and thus not seen as a problem.

A Markov chain Monte Carlo (MCMC) method is used to first sample the probability distributions of the geoacoustic parameters. Unlike previous research, the results of the geoacoustic inversion are only an intermediate goal. Subsampling of the multidimensional model parameter distribution is then used to map parameter uncertainties to the TL domain. In

Ref. 14, exhaustive grid sampling was used to obtain the geoacoustic uncertainties and map these to the TL domain. This was feasible because only 4 model parameters were explored. However, a more realistic inversion will have a large number of parameters. In this paper we invert for a total of 13 model parameters and also validate the estimated transmission loss with at-sea observations.

Figure 1 summarizes the estimation of TL (usage domain \mathcal{U}) from ocean acoustic data observed on a vertical or horizontal array (data domain \mathcal{D}).¹⁴ The geoacoustic inverse problem is solved as an intermediate step to obtain the posterior distribution of environmental parameters $p(\mathbf{m}|\mathbf{d})$ (environmental domain \mathcal{M}). We are not directly interested in the environment itself but rather a statistical estimation of the TL field (usage domain \mathcal{U}). Based on the posterior distribution $p(\mathbf{m}|\mathbf{d})$, the probability distribution of the transmission loss $p(\mathbf{u}|\mathbf{d})$ is obtained via Monte Carlo integration. From this TL probability distribution, all relevant statistics of TL can be obtained, such as the median, percentiles, and correlation coefficients.

Both the experimental data \mathbf{d} and the usage domain model \mathbf{u} are related to \mathbf{m} via forward models $\mathbf{D}(\mathbf{m})$ and $\mathbf{U}(\mathbf{m})$, respectively. Thus formally, if the data were error free and the mappings were unique, we would have $\mathbf{u} = \mathbf{U}(\mathbf{D}^{-1}(\mathbf{d}))$. It is assumed that the mappings $\mathbf{D}(\mathbf{m})$ and $\mathbf{U}(\mathbf{m})$ are deterministic and all uncertainties (including noise and modeling errors) are in the data. Due to the uncertainties in the data, the inverse mapping from \mathbf{d} to \mathbf{m} is formulated in a probabilistic framework where one also can include prior information. The forward mapping could be probabilistic as in the textbook by Tarantola¹⁵ and in the papers by Mosegaard and Tarantola¹⁶ and Rogers *et al.*¹⁷

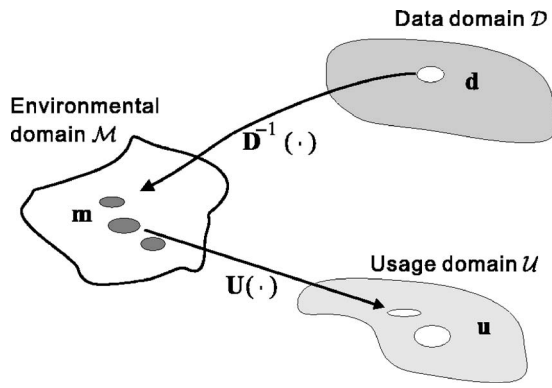


FIG. 1. An observation \mathbf{d} ($\in \mathcal{D}$) is mapped into a distribution of environmental parameters \mathbf{m} ($\in \mathcal{M}$) that potentially could have generated it. These environmental parameters are then mapped into the usage domain \mathcal{U} .

II. BAYESIAN INFERENCE

In the Bayesian paradigm, the solution to estimating parameters of interest \mathbf{m} given an observation \mathbf{d} is characterized by the posterior probability $p(\mathbf{m}|\mathbf{d})$. First, the prior information about the model parameter vector is quantified by the probability density function (pdf) $p(\mathbf{m})$. Then, this information is combined with the likelihood function $p(\mathbf{d}|\mathbf{m})$ provided by the combination of data and the physical model to give the posterior information of the model parameters $p(\mathbf{m}|\mathbf{d})$. A complete discussion of inverse theory from a probabilistic point of view may be found in the recent textbook by Tarantola.¹⁵ The solution to the inverse problem is then

$$p(\mathbf{m}|\mathbf{d}) = \frac{p(\mathbf{d}|\mathbf{m})p(\mathbf{m})}{p(\mathbf{d})} \propto \mathcal{L}(\mathbf{m})p(\mathbf{m}), \quad (1)$$

where $p(\mathbf{d})$ is a normalizing factor that makes the posterior probability density $p(\mathbf{m}|\mathbf{d})$ integrate to one. Since $p(\mathbf{d})$ does not depend on the environmental model \mathbf{m} , it typically is ignored in parameter estimation. Hence, as shown in the second representation, the normalization constant $p(\mathbf{d})$ is omitted and a brief notation $\mathcal{L}(\mathbf{m})$ is used to denote the likelihood function $p(\mathbf{d}|\mathbf{m})$.

Understanding and using the posterior distribution $p(\mathbf{m}|\mathbf{d})$ is at the heart of Bayesian inference. Specifically, one is interested in various features of the posterior distribution, such as the means, variances, and marginal distributions. These quantities can be written as expectations of functions $f(\mathbf{m})$ under $p(\mathbf{m}|\mathbf{d})$ as follows:

$$E[f(\mathbf{m})] = \int_{\mathcal{M}} f(\mathbf{m})p(\mathbf{m}|\mathbf{d})d\mathbf{m}. \quad (2)$$

For example, if the desired statistical quantity is the marginal posterior distribution of the parameter m_i , then

$$p(m_i|\mathbf{d}) = \int_{\mathcal{M}} \delta(m'_i - m_i)p(\mathbf{m}'|\mathbf{d})d\mathbf{m}'. \quad (3)$$

A. Data model

This section derives a likelihood function to be used in the probabilistic inversion following the same approach as

described in Gerstoft and Mecklenbräuker.^{2,18} At a single frequency, the relation between the observed complex-valued data vector \mathbf{d} sampled at an N -element array and the modeled data $\mathbf{D}(\mathbf{m})$ is described by the model

$$\mathbf{d} = \mathbf{D}(\mathbf{m}) + \mathbf{e}, \quad (4)$$

where \mathbf{e} represents the error term. The modeled data are given by $\mathbf{D}(\mathbf{m}) = \mathbf{d}(\mathbf{m})s$, where the complex deterministic source term s is unknown. The transfer function $\mathbf{d}(\mathbf{m})$ is obtained using an acoustic propagation model for an environmental model \mathbf{m} .¹⁹ For simplicity in the development, data from only one frequency is assumed.

Assume the errors \mathbf{e} to be Gaussian distributed with zero mean and covariance \mathbf{C}_e . The errors represent all features that are not modeled in the data such as noise, theoretical errors, and modeling errors.^{2,7,15} Hence, the likelihood function is

$$\mathcal{L}(\mathbf{m}, \mathbf{C}_e, s) = \frac{1}{\pi^N |\mathbf{C}_e|} \exp(-[\mathbf{d} - \mathbf{d}(\mathbf{m})s]^\dagger \mathbf{C}_e^{-1} [\mathbf{d} - \mathbf{d}(\mathbf{m})s]), \quad (5)$$

where N is the number of data points and superscript \dagger denotes the complex conjugate transpose. Although in general not true, an independent and identically distributed (IID) error process $\mathbf{C}_e = \nu \mathbf{I}$ is assumed to describe the data uncertainty. The source term s can be estimated in closed form by requiring $\partial \log \mathcal{L} / \partial s = 0$, whereby

$$s_{\text{ML}} = \frac{\mathbf{d}^\dagger(\mathbf{m})\mathbf{d}}{\|\mathbf{d}(\mathbf{m})\|^2}. \quad (6)$$

It is seen that s depends on \mathbf{m} but not on ν . After substituting s_{ML} back into Eq. (5), the likelihood function is then

$$\mathcal{L}(\mathbf{m}, \nu) = \frac{1}{\pi^N \nu^N} \exp\left(-\frac{\phi(\mathbf{m})}{\nu}\right), \quad (7)$$

where

$$\phi(\mathbf{m}) = \|\mathbf{d}\|^2 - \frac{|\mathbf{d}^\dagger(\mathbf{m})\mathbf{d}|^2}{\|\mathbf{d}(\mathbf{m})\|^2} \quad (8)$$

is the objective function. Here, we treat the error variance ν as a nuisance parameter and eliminate it via integrating Eq. (7) weighted by a noninformative prior of ν [$p(\nu) = 1/\nu$] over its entire range²⁰

$$\mathcal{L}(\mathbf{m}) = \int_0^\infty \mathcal{L}(\mathbf{m}, \nu)p(\nu)d\nu. \quad (9)$$

Therefore, the likelihood function can be written as

$$\mathcal{L}(\mathbf{m}) = \frac{1}{\pi^N} \frac{(N-1)!}{\phi(\mathbf{m})^N}. \quad (10)$$

It is straightforward to extend the above formula to the multifrequency data set²⁰

$$\mathcal{L}(\mathbf{m}) \propto \left[\frac{1}{\bar{\phi}^s(\mathbf{m})} \right]^{NJ} = [\prod \phi_j(\mathbf{m})]^{-N}, \quad (11)$$

where J is the number of processed frequencies and $\bar{\phi}^s(\mathbf{m}) = \sqrt{J} \prod \phi_j(\mathbf{m})$ is the geometric mean of the objective function over frequency.

The above derivation assumes that the errors are independent across both spatial samples of the acoustic field and frequencies. In practice these can be strongly correlated, for example, when the errors due to frequency-dependent modeling mismatch are the dominant source of error, the modeling error may not be independent across the frequencies used. Therefore, the number of independent samples NJ in Eq. (11) must be selected with care (see Sec. III B for details).

B. Prediction

A related problem is to infer what experimental values are likely to be observed given our knowledge of the environmental parameters. Thus, we are not just interested in the environment itself but also estimates in the information usage domain \mathcal{U} (Fig. 1). In the present application, the usage domain is transmission loss (TL). The vector \mathbf{u} is used to denote the transmission loss at I discrete positions, $u_i = u(r_i, z_i)$. For the example in Sec. III, we predicted the TL field on a 200×100 grid of range-depth cells, $I=200 \times 100 = 20\,000$, inferred from a 13-dimensional model \mathbf{m} .

Probability density functions that describe yet unobserved events are referred to as predictive distributions. Based on the posterior distribution $p(\mathbf{m}|\mathbf{d})$, the posterior predictive distribution $p(\mathbf{u}|\mathbf{d})$ is obtained from the joint posterior pdf of \mathbf{u} and \mathbf{m} given \mathbf{d} ,

$$p(\mathbf{u}|\mathbf{d}) = \int_{\mathcal{M}} p(\mathbf{u}, \mathbf{m}|\mathbf{d}) d\mathbf{m} = \int_{\mathcal{M}} p(\mathbf{u}|\mathbf{m}, \mathbf{d}) p(\mathbf{m}|\mathbf{d}) d\mathbf{m}, \quad (12)$$

where the second equation follows from the definition of conditional probability. Since all uncertainties are assumed to be in the data \mathbf{d} and all information in \mathbf{d} has been mapped into \mathbf{m} (see Fig. 1 and the discussion in the last paragraph of Sec. I), conditioning on \mathbf{d} adds no information in our prediction of \mathbf{u} . Therefore,

$$p(\mathbf{u}|\mathbf{m}, \mathbf{d}) = p(\mathbf{u}|\mathbf{m}). \quad (13)$$

The conditional probability density $p(\mathbf{u}|\mathbf{m})$ is used to describe uncertainties in the forward mapping due to imperfect knowledge of the environment (e.g., parametrization).¹⁵⁻¹⁷ Here, the forward mapping is assumed exact: a functional relationship $\mathbf{u}=\mathbf{U}(\mathbf{m})$ gives the transmission loss \mathbf{u} exactly for each value of \mathbf{m} . Note that $\mathbf{u}=\mathbf{U}(\mathbf{m})$ is a short notation for the set of equations $u_i=U_i(\mathbf{m})$, $i=1, \dots, I$. Therefore, the probability density is

$$p(\mathbf{u}|\mathbf{m}) = \delta(\mathbf{U}(\mathbf{m}) - \mathbf{u}), \quad (14)$$

where the vector delta function is defined as the product of the delta functions for the elements^{15,21} as in

$$\delta(\mathbf{U}(\mathbf{m}) - \mathbf{u}) = \prod_{i=1}^I \delta(U_i(\mathbf{m}) - u(r_i, z_i)). \quad (15)$$

The posterior predictive distribution of \mathbf{u} for a set of discrete ranges and depths given the observed acoustic data \mathbf{d} is obtained by integrating the values of the TL with respect to the posterior distribution of the model parameters

$$p(\mathbf{u}|\mathbf{d}) = \int_{\mathcal{M}} \delta(\mathbf{U}(\mathbf{m}) - \mathbf{u}) p(\mathbf{m}|\mathbf{d}) d\mathbf{m} \quad (16)$$

which has the same form as Eq. (2). As shown in the Appendix, this is a generalization of the transformation of random variables using the properties of the Dirac delta function. However, in the present case, neither the roots nor the derivatives are known, and thus it is easier to implement Eq. (16) directly as described in Sec. II C.

The posterior distribution $p(\mathbf{u}|\mathbf{d})$ carries all the information about the TL in the presence of the geoacoustic inversion uncertainties. As the predictive distributions are not necessarily Gaussian, it is preferable to characterize the distributions with medians and distance between the 5th and 95th percentiles instead of means and standard deviations. Note that the median corresponds to the 50th percentile of the distribution. The β th percentile of the TL distribution at a given position, denoted by $u^{\beta\%}$, is computed by finding the TL value that satisfies

$$\int_{-\infty}^{u^{\beta\%}} p(u|\mathbf{d}) du = \beta/100. \quad (17)$$

In addition to summarizing the statistics of TL at any particular point, the covariance structure of the TL at two points might also be of interest in uncertain acoustic environments. From Eq. (16), the covariance and correlation coefficient between the TL at two positions u_i and u_j can be computed, respectively, by

$$\text{cov}(u_i, u_j) = E[u_i u_j] - E[u_i] E[u_j] \quad (18)$$

and

$$R_{ij} = \frac{\text{cov}(u_i, u_j)}{\sqrt{\text{cov}(u_i, u_i)} \sqrt{\text{cov}(u_j, u_j)}}. \quad (19)$$

To compute the above statistical quantities of TL, one needs to evaluate the high-dimensional integral of Eq. (16). The integral can be approximated numerically as described in the next section.

C. Markov chain Monte Carlo method

Monte Carlo methods can evaluate integrals in high-dimensional space efficiently.²² In particular, Markov chain Monte Carlo (MCMC) algorithms have been found to be well suited for problems of Bayesian inference. The commonly used MCMC methods are the Metropolis-Hastings algorithm, which was introduced first in Ref. 23, and Gibbs sampling which was developed originally in Ref. 24 where it was applied to image processing. MCMC are extensively

used in various fields of inverse problems, such as geophysics,^{16,25} ocean acoustics,^{7,26,27} and electromagnetics.²⁸ MCMC algorithms consist of a random walk in the parameter space where the next parameter value depends only on the current value. After an initial “burn-in” period in which the random walker moves toward the high posterior probability region, the chain samples a desired posterior pdf, that is, it returns a number of parameter vectors that are distributed as in the posterior pdf.

In the MCMC, samples are generated from the posterior distribution $p(\mathbf{m}|\mathbf{d})$. The difficult part is to create a Markov chain which converges rapidly. As noted by many authors,^{7,29,30} parameter coupling frequently is encountered in ocean acoustics. High correlation between parameters can slow down the convergence of a MCMC sampler considerably. Thus, a parameter covariance matrix estimated from the sampled models during the initial “burn in” period⁷ is used for determining appropriate coordinate rotations.

MCMC convergence was established by collecting two independent runs in parallel and periodically comparing the marginal distributions of the parameters estimated from each run.⁷ The procedure is terminated when the maximum difference between two cumulative marginal distributions for all parameters is less than 0.05. A good introduction to MCMC methods is in Ref. 31, which also contains many applications in statistical data analysis.

The integral in Eq. (16) is the expectation of function $\delta(\mathbf{U}(\mathbf{m})-\mathbf{u})$ with respect to the posterior distribution of the model parameters. This and other expectations can be approximated by using the MCMC samples $\{\mathbf{m}^{(t)}\}$ drawn from the posterior distribution of model parameters $p(\mathbf{m}|\mathbf{d})$

$$p(\mathbf{u}|\mathbf{d}) = \frac{1}{T} \sum_{t=1}^T \delta(\mathbf{U}(\mathbf{m}^{(t)}) - \mathbf{u}), \quad (20)$$

where the superscript t is used to label the sequence of states in a Markov chain and T denotes the total length of the sequence. To implement Eq. (20), a numerical approximation is made by binning the calculated TL values. The bin width is selected small enough to have negligible effect on the distribution. Here a 1 dB bin width is used.

Using all samples from MCMC runs can consume a large amount of storage to save all $\mathbf{m}^{(t)}$ and computation time to compute $p(\mathbf{u}|\mathbf{d})$. It has been suggested in the statistical literature³¹⁻³³ that inferences should be based on a subsampling of each sequence, with a subsampling factor high enough that successive draws of \mathbf{m} are approximately independent. The strategy is known as *subsampling*.³³ This can save a large amount of storage and computation time for using the MCMC samples in inference. This subsampling reduces the number of samples needed to calculate $p(\mathbf{m}|\mathbf{d})$ and thus translates into a large saving in computer time for calculating $p(\mathbf{u}|\mathbf{d})$. Practically, we use a Monte Carlo (random) subsampling of the MCMC samples $\{\mathbf{m}^{(t)}\}$ and monitor the convergence of the maximum difference between the marginal cumulative distributions estimated from subsamples and from all MCMC samples. This maximum difference should be less than 0.05 for all parameters. Then

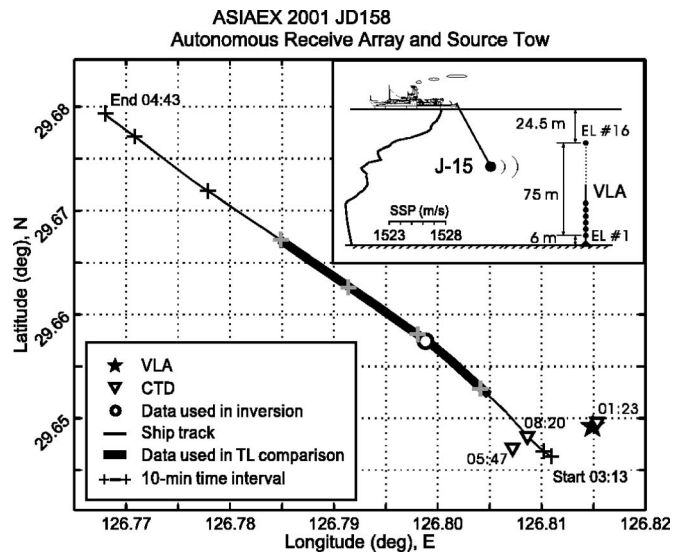


FIG. 2. Track of R/V *Melville* during the ASIAEX 2001 East China Sea experiment. The experimental geometry is shown in the upper right-hand corner of the figure.

these subsampled model parameter vectors are used to compute $p(\mathbf{u}|\mathbf{d})$.

All results presented in this paper are generated by SAGA,³⁴ which implements the method described in Ref. 28.

III. RESULTS AND DISCUSSION

Data from the ASIAEX 2001 East China Sea experiment³⁵ are used to illustrate the approach. Figure 2 shows a map of the region where the acoustic measurements were taken. On Julian Day (JD) 158, acoustic energy was transmitted from the J-15 source towed near 48 m depth by R/V *Melville* with a speed of about 3 knots. The ship track is indicated by the line in the figure on which the distances between the source and the receiver range from 0.5 to 6 km. The experiment geometry is illustrated schematically in Fig. 2. A 16-element, 75-m aperture, autonomous recording vertical line array (VLA) was moored up from the seafloor at location 29° 38.927' N, 126° 48.892' E where the measured water depth was approximately 105.5 m. The lowermost element (element 1) was about 6 m above the bottom. Element 4 failed during deployment.

For oceanographic measurements, the current profile in the water column from 30 to 100 m was obtained by a ship-mounted ADCP system. During the acoustic transmissions, there exists a strong tidal current with magnitude greater than 0.5 m/s around the middle of the water column. Three sound speed profiles were measured by CTDs on JD 158. As shown in Fig. 2, typical summer sound speed profile characteristics were observed with significant fluctuations in the thermocline.

A general bathymetric and geological survey has indicated that in the neighborhood of the experimental site, the environment is nearly range independent. Additional details of the seismic and oceanographic experiments can be found in Ref. 35.

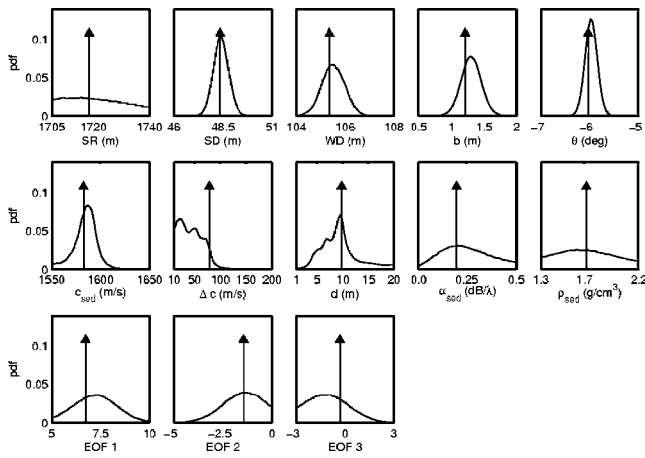


FIG. 3. 1D marginal posterior probability densities of the model parameters using the measured data obtained at approximately 1.7 km from the source. Arrows indicate the estimated optimum values of the parameters.

A. Baseline model

The baseline model is assumed to be range-independent and consists of an ocean layer overlying a uniform sediment layer on top of a subbottom. The model parameters were divided into three subsets: geometrical, geoacoustic, and ocean sound speed parameters. The geometrical parameters include source range SR, source depth SD, water depth WD, and the array shape (array tilt θ and bow b). The geoacoustic parameters include sediment compressional speed c_{sed} , density ρ_{sed} , attenuation α_{sed} , and thickness d , and increment of subbottom compressional speed from the top sediment layer Δc (subbottom density and attenuation are fixed at 2.4 g/cm^3 and $0.01 \text{ dB}/\lambda$, respectively). The ocean sound speed was modeled by a linear combination of empirical orthogonal functions (EOFs). An empirical orthogonal function (EOF) analysis at the experimental site shows that the first 3 EOFs contain about 90% of the energy. Therefore, the number of representative EOFs was set to three in the inversion.

An environmental domain of 13 parameters with their search bounds is indicated in Fig. 3, including (from upper to lower panels) geometrical, geoacoustic, and ocean sound speed EOF coefficients.

B. Posterior distributions for the model parameters

Matched-field (MF) geoacoustic inversion using the selected frequencies 195, 295, and 395 Hz was carried out with the measured data obtained at approximately 1.7 km from the source (the circle in Fig. 2). The MCMC algorithm along with the normal-mode propagation model SNAP (Ref. 19) is employed to sample the posterior probability density in model domain \mathcal{M} .

Figure 3 shows the marginal posterior distributions of the model parameters using the likelihood function, Eq. (11) with the number of independent samples, NJ , found as follows. First, the data error covariance matrix C_e is estimated using a maximum-likelihood approach. It is based on an ensemble average of the residual vectors (residual field between the observed and the modeled field generated from the optimum values of the parameters) from multiple inversions of vertical array data from a source tow.³⁶ For each source

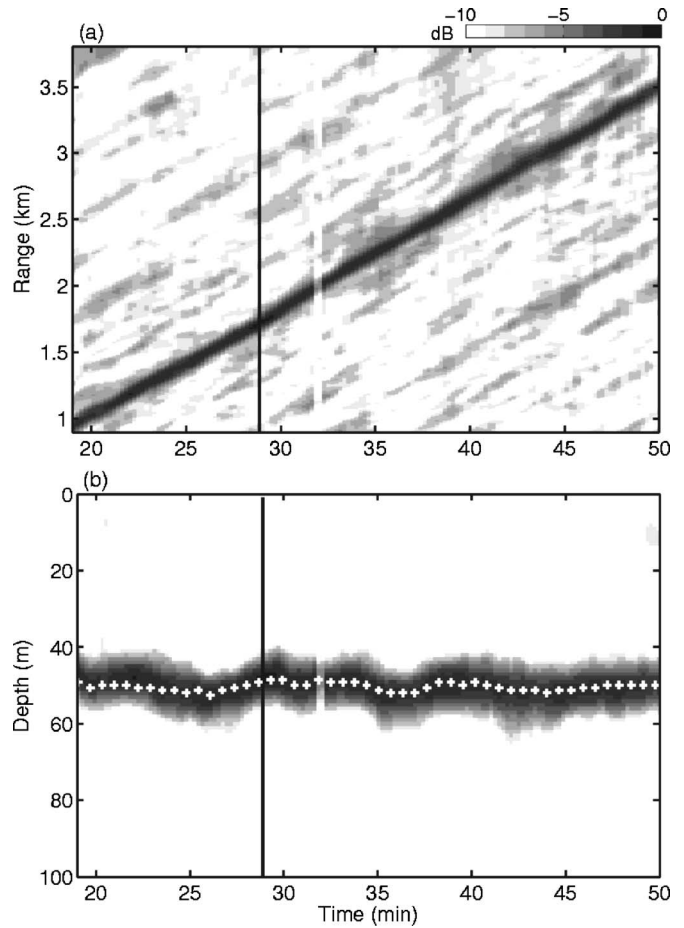


FIG. 4. MF-derived (a) source-receiver range and (b) source depth over the time interval from 19 to 50 min. The contour plots show the MF output (dB) where the best match for each time sample is 0 dB. The vertical line on each plot indicates where the environmental model is estimated. Plus signs indicate the true measured source depths.

range, the residual vectors of processed frequencies are concatenated creating an error vector consisting of $15 \times 3 = 45$ entries (15 hydrophone elements by 3 frequencies). A total of 98 error vectors are used to estimate C_e . Then, to find the number of independent samples NJ , the eigenvalue analysis is performed on the estimated C_e . The result shows there are 30 significant eigenvalues, containing 99.9% of the energy, in the error covariance matrix. Therefore, the number of independent samples, NJ , for this analysis, is 30.

Figure 4 shows the MF-derived source position over the time interval from 19 to 50 min using the estimated optimum values of the parameters found from the above inversion. The source depths measured by the depth sensor are indicated by the plus signs. Compared with the GPS and the depth sensor measurements, MF-derived source position is consistent with the experimental configuration. Source localization based on the best-fit model tracks the actual source positions well.

C. Predictive distributions of transmission loss

With the posterior probability density of the environmental model parameters obtained from the inversion, we quantify the uncertainty mapped from the model parameters to the predicted transmission loss (TL). The posterior predic-

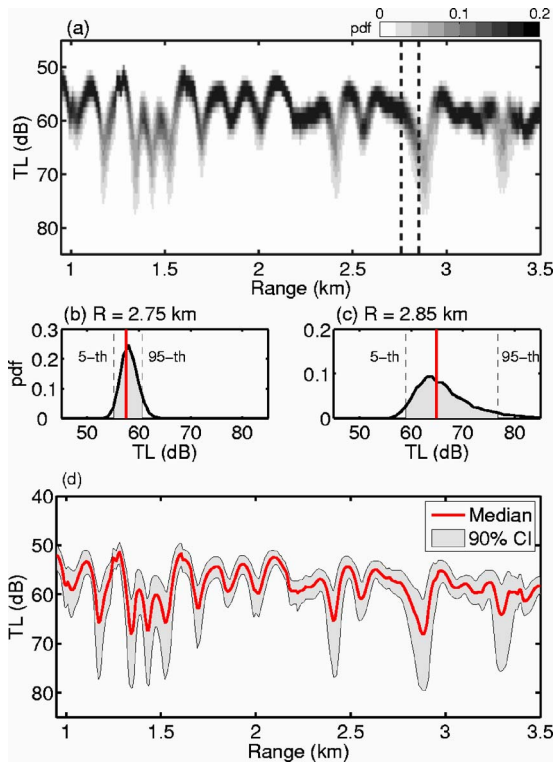


FIG. 5. (Color online) Posterior distribution of TL versus range for 295 Hz for array element 7 (at 69.5 m): (a) Contour of posterior distribution for TL versus range. (b) and (c) Posterior distributions of TL at two different ranges (2.75 km and 2.85 km). These corresponds to cuts (vertical dashed lines) through the contour. (d) Statistics of the predicted TL versus range. The solid line with gray area around shows the median and the 90% interval of posterior distribution.

tive distribution of TL for the position (r_i, z_i) is obtained by integrating the predictions of TL with respect to the posterior distribution of the model parameters, using Eq. (16).

Figure 5 shows the posterior distribution of the TL versus range at 295 Hz for array element 7 (at 69.5 m). Figure 5(a) shows the contour of the predictive distribution of the TL versus range. Gray levels represent the probability density. Darker shades mean higher probability of observing the predicted TL value. It is observed that at some ranges where the acoustic field is near a null (destructive interference), the predictive probabilities show large variations in the result.

Predictive distributions at two different ranges are shown in Figs. 5(b) and 5(c), which correspond to the points of constructive and destructive interferences, respectively. At the range of constructive interference [Fig. 5(b)], less variation of TL is observed. Therefore, the probability density concentrates in a smaller area. However, near the range of destructive interference [Fig. 5(c)], the probability density spreads in a larger area which indicates the acoustic field is more difficult to predict. Since the distribution of TL is often poorly approximated by a normal distribution, particularly near destructive interferences, the central tendency and spread of the TL distribution are indicated, respectively, by the median (heavy vertical line) and the distance between the 5th and 95th percentiles (gray area; referred to as the 90% Credibility Interval). Figure 5(d) summarizes the predictive

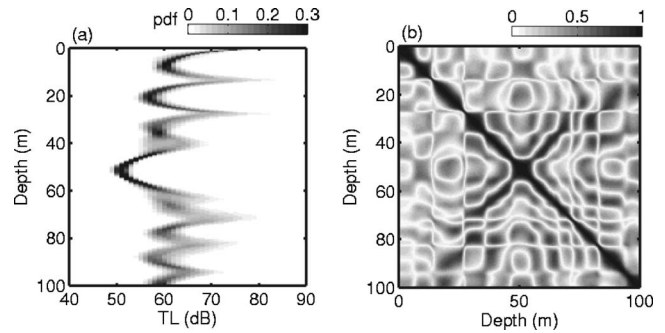


FIG. 6. Posterior probability distribution of TL versus depth for 295 Hz at the 2.85 km range: (a) Contour of posterior probability distribution for TL versus depth. (b) Magnitude of the correlation coefficient matrix for TL at all depths.

distributions by the median (heavy line) and the 90% CI (gray area). This is a practical way to convey the uncertainty in TL.

Figure 6 shows the posterior distribution of TL versus depth for 295 Hz at 2.85-km range. Figure 6(a) shows the contour of posterior probability distribution for TL versus depth. We see a similar constructive/destructive interference pattern as observed in the range contour of the TL distribution. The vertical covariance structure of the TL is examined in Fig. 6(b). Due to the interference of the normal modes, a chessboardlike correlation structure of the TL is observed. For regions near the constructive interference (for example, at a depth of 50 m), the TL is correlated more at neighboring depths. For regions near destructive interference (at 81 m depth), the correlation drops rapidly.

To demonstrate the correlation structure in detail, Fig. 7 shows the 2D posterior probability distributions between TL

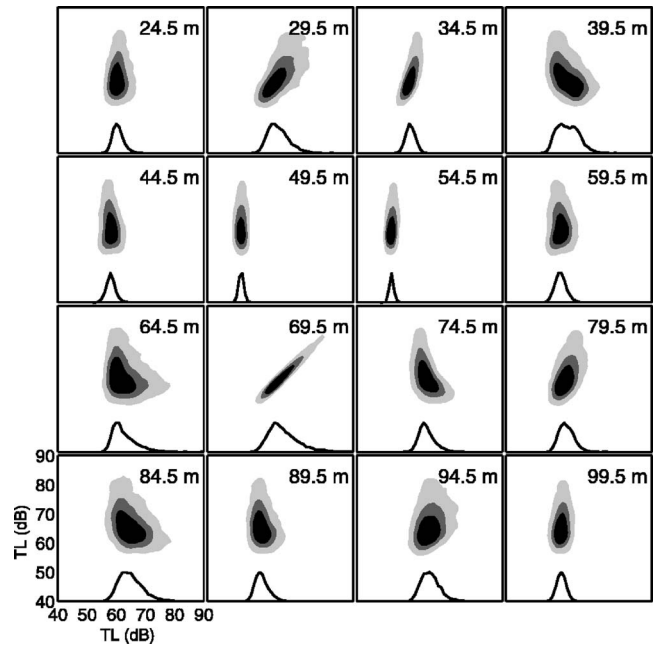


FIG. 7. 2D posterior probability distribution of TL versus depth for 295 Hz at the 2.85 km range. The vertical and horizontal axes indicate, respectively, the TL field at 69.5 m depth and that at the depth indicated on each panel. The gray-scale coloring from darkest to lightest represents 50%, 75%, and 95% highest posterior density (HPD) (Ref. 20). 1D posterior probability distribution of TL at that depth is also shown on the bottom of each panel.

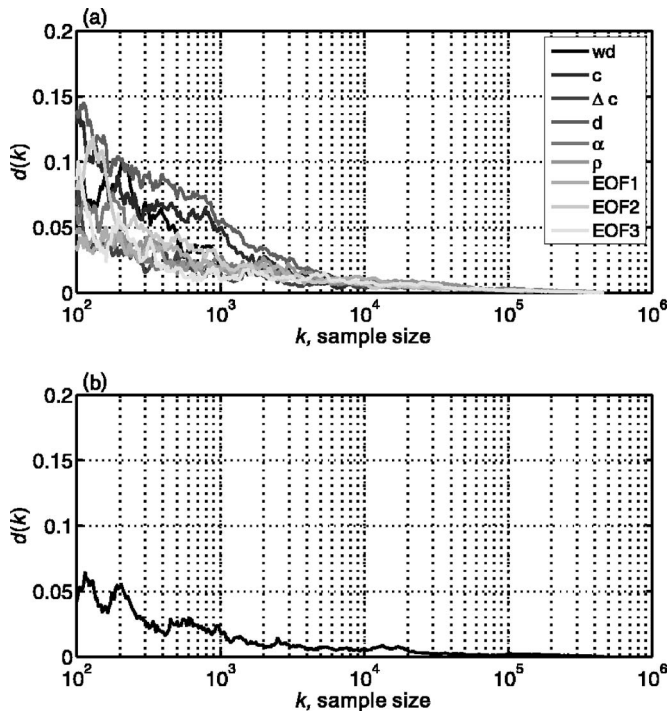


FIG. 8. Convergence of (a) the posterior probability distribution of each model parameter and (b) the predictive probability distribution of the TL at 69.5 m depth and 2.85 km range [see Fig. 5(c) for the distribution]. The vertical axis indicates the maximum difference between the cumulative distributions of k -length subsamples and the cumulative distribution of the full MCMC samples (the length of 480 000).

at 69.5 m depth (vertical axis) and TL at selected depths (horizontal). Gray levels represent the probability density; darker shade means higher probability density. The line plot on the bottom of each panel is the marginal distribution of TL at the corresponding depth, which corresponds a cut through Fig. 6(a) at that corresponding depth.

As discussed in Sec. II C, significant saving in both storage and computation time can be obtained by subsampling MCMC samples. Note that about 480 000 samples were required for the MCMC to converge. Figure 8(a) shows the convergence of the Monte Carlo subsampling for each model parameter. We find that about 10 000 samples are sufficient to characterize the marginal distributions of model parameters.

As an indication of convergence for TL distribution, we computed the marginal distributions of TL for the subsampled model parameter vectors. Figure 8(b) shows convergence for the marginal probability distributions of TL at 69.5 m depth and 2.85 km range, which corresponds to a long tail distribution as shown in Fig. 5(c). Similar to sampling the marginal distributions of model parameters, 10 000 samples can capture accurately the predictive distribution of the TL at this chosen position (with maximum error 0.025).

D. Experimental comparisons

We have demonstrated how to estimate the statistical properties of the TL in the presence of uncertainty embedded in the environmental model parameters. To further illustrate the versatility and usefulness of the predictive distributions of the TL, the resulting statistics are compared with actual TL observations.

Bayesian inference gives us the posterior distribution of the full parameter vector. To estimate the statistical properties of the TL, only the posterior distribution of geoacoustic parameters and ocean sound speed EOFs is required, but not the distribution of the geometric parameters. The environmental parameters are the geoacoustic parameters, ocean sound speed EOF coefficients, and water depth (water depth is included since it affects the number of propagating modes in the waveguide). Uncertainties in these parameters can be obtained easily by integration over the remaining geometric parameters, that is, simply removing these variables (SD, SR, b , and θ) from the parameter vector.

Source depth is an important parameter for predicting TL fields accurately. In this data set, the depth sensor measurement indicates that the source varied between 48 and 52 m. Since the measured and MF estimated source depths (as shown in Fig. 4) are virtually the same, the MF-derived time-varying source position is included in the TL prediction, referred to as the MFSD model.

Figure 9 compares the observed TL (dots) with the predicted TL statistics of the MFSD model (solid line with gray area) for the frequencies 195, 295, and 395 Hz (left to right) and for array elements 1, 7, and 16 (bottom to top; depths at 99.5, 69.5, and 24.5 m). We see that for 195 Hz the TL uncertainty band is about 5 dB near the ranges of constructive interference and is widened near the ranges of destructive interference. As frequency increases, larger spreads in TL predictions are observed. This is most pronounced near regions of destructive interference. In general, the predicted TL patterns using the MFSD model follow the trends of the measured TL well. Table I summarizes comparisons of measured and predicted TL from Fig. 9. As frequency increases, the uncertainty band of the predicted TL (number in dB) increases by approximately 3 dB and more of the observed TL points are within the 90% CI.

To investigate the effect of the source depth uncertainty, we have estimated the TL distributions for 295 Hz for the following three additional cases:

- (1) The marginal posterior distribution of source depth obtained from the 1.7 km inversion is assumed for all ranges, referred to as the SD@1.7 km model.
- (2) The range-dependent source depth variability is accounted for by the statistics of the measured source depth. The parameter SD is treated as a random variable having the mean value of 50.2 m and standard deviation of 1.5 m, estimated from the measured source depths. At each range, the source depth is a Gaussian distribution centered at 50.2 m with uncertainty band of 1.5 m, referred to as the MEAN+STD model.
- (3) The uncertainty band in the MEAN+STD model is applied to the MFSD model. At each range, the source depth is assumed to be a Gaussian distribution centered at the MF-derived source depth with standard deviation of 1.5 m, referred to as the MEAN+STD model.

Figure 10 shows comparisons of predicted and measured TL for the above described source depth distribution models

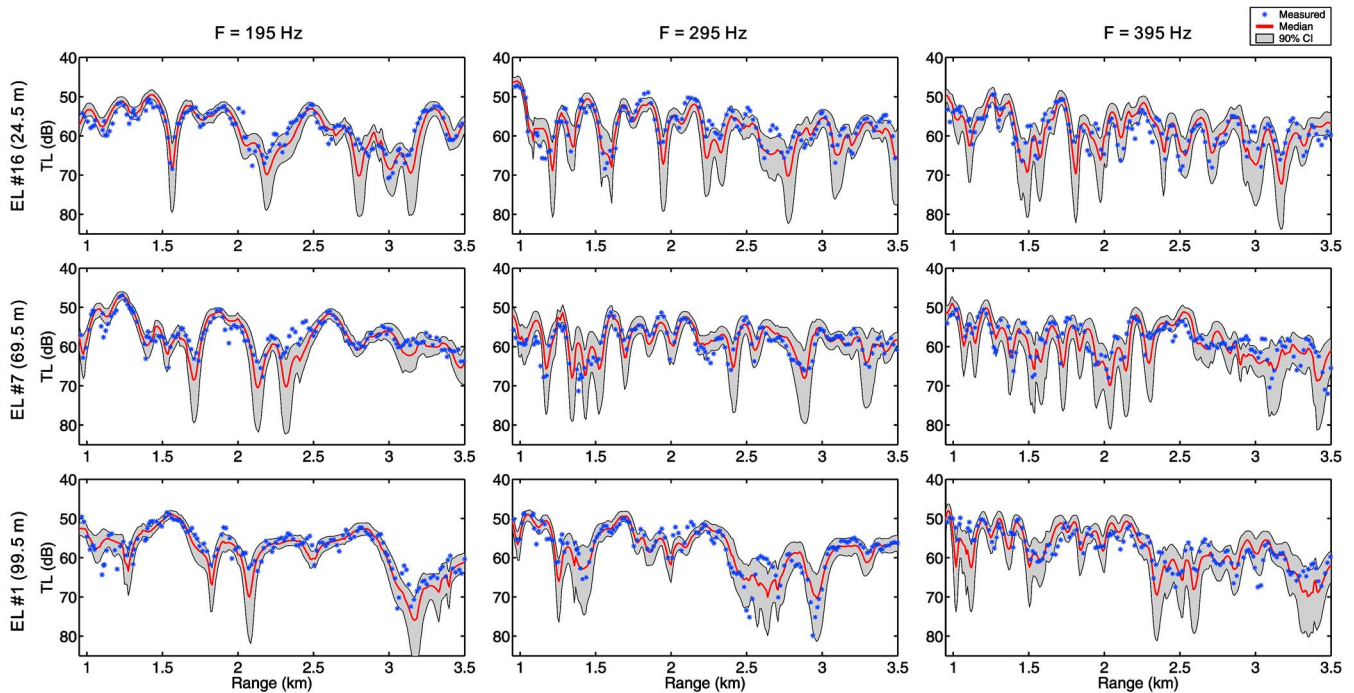


FIG. 9. (Color online) Predicted and measured TL (dots) for array elements 1, 7, and 16 and for frequencies 195, 295, and 395 Hz. The median of the predicted TL (solid line) is shown together with the 90% CI (gray area). The source depth is estimated from MF processing.

for a frequency of 295 Hz. The prediction quality is summarized in Table I. The results using the marginal posterior distribution of the source depth obtained at the 1.7 km range (left column) show that the prediction quality is rather poor. For instance, for array element 7 (middle row) the constructive interference region near 1.6 km and the destructive interference region near 2.2 km are not captured by the predictions. This is expected since the source depth at each range differs substantially from the estimated source depth at the range of 1.7 km. For the MEAN+STD model (middle column), we see that the fine scale features of the observed TL are matched by the predictions. Compared with the MFSD model (middle column in Fig. 9), the addition of source depth uncertainty results in the TL uncertainty band being much wider. The predicted TL patterns follow the trends of the measured TL well. For the MFSD+STD model (right column), it shows the highest percentage of the observed TL inside the CI. Table I shows that the median value of predicted TL spread increases by approximately 3 dB more than the MFSD alone, and about 7%–11% more of the observed TL points fall within the gray area.

We found that, in general, about 80% of the observed TL

data falls within the predicted 90% CI. Since the predicted TL statistics are derived from uncertainty in geoacoustic parameters $p(\mathbf{m}|\mathbf{d})$ for the given environmental parameterization only (we assume a range-independent environment). Complicated environments, such as spatial and temporal fluctuations in the water column, sediment, sea surface, and water-sediment interface, are not modeled and this will increase the error. Further, all noise sources have not been taken into account. Therefore, the percentage of observed data points inside the computed CI is less than the predicted.

IV. CONCLUSION

This paper investigates the statistical estimation of TL based on the posterior probability density of environmental parameters obtained from the geoacoustic inversion process. First, a Markov chain Monte Carlo procedure is employed to sample the posterior probability density of the geoacoustic parameters. Then, these parameter uncertainties are mapped to the transmission loss domain where a full multidimensional probability distribution of the TL as a function of

TABLE I. Summary of TL prediction performance. Numbers in dB indicate the median value of the predicted TL spread over all range, while numbers in % represent the percentage of the measured TL points that lie inside the 90% CI.

Element number (depth)	MFSD (Fig. 9)			$F=295$ Hz (Fig. 10)		
	195 Hz	295 Hz	395 Hz	SD@1.7 km	MEAN+STD	MESD+STD
16 (99.5 m)	4.9 dB/73%	6.2 dB/80%	7.7 dB/82%	7.2 dB/61%	11 dB/88%	9.6 dB/91%
7 (69.5 m)	4.3 dB/73%	6.1 dB/85%	8.2 dB/79%	7.3 dB/69%	9.6 dB/93%	9.3 dB/92%
1 (24.5 m)	4.6 dB/69%	5.4 dB/80%	7.8 dB/81%	4.9 dB/67%	6.9 dB/85%	7.4 dB/91%

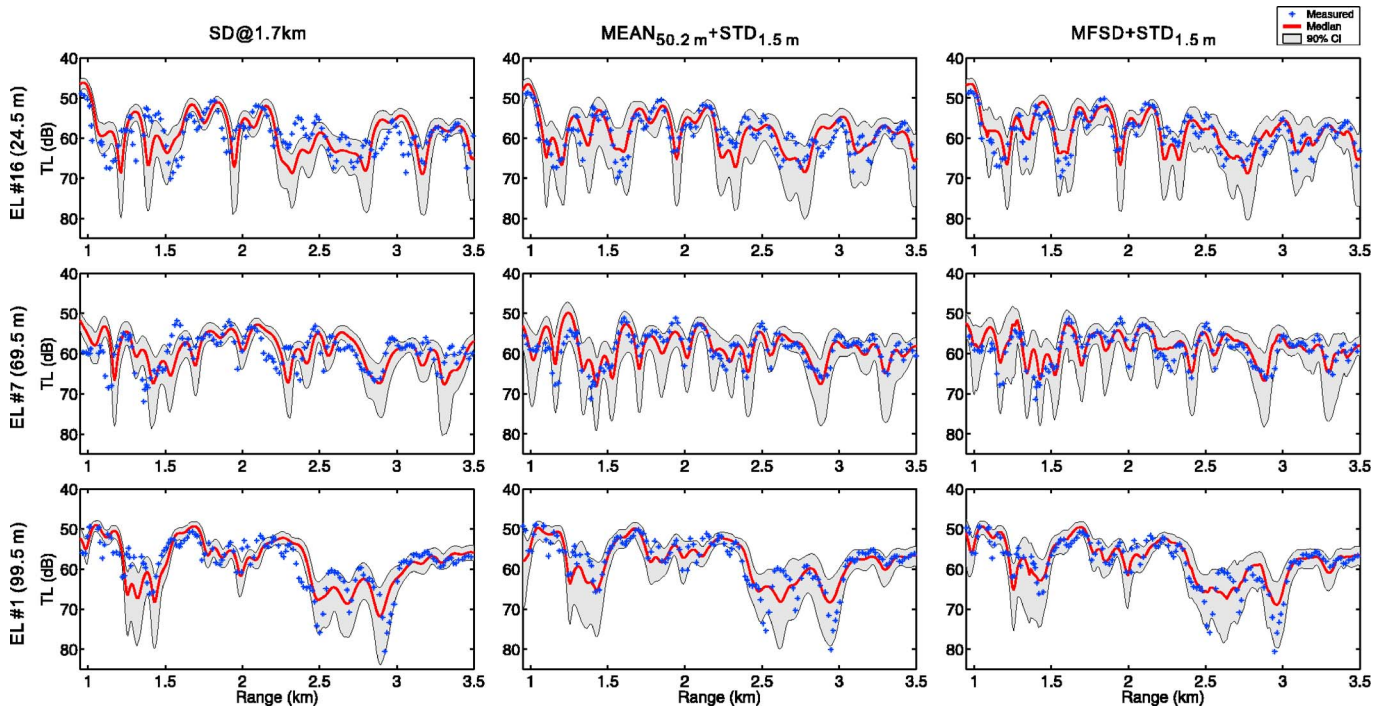


FIG. 10. (Color online) Predicted and measured TL for 295 Hz for various source depth distribution models. Left column (SD@1.7 km): the source depth is inferred from the inversion at 1.7 km; Middle column (MEAN+STD): fixed source depth (50.2 m) with the standard deviation (1.5 m); Right column (MFSD+STD): MF-derived source depth with 1.5-m standard deviation.

range and depth is obtained. The summary statistics of predicted TL including the median, percentiles, and correlation coefficients are considered.

A Monte Carlo subsampling technique is applied to subsample the full MCMC model parameter samples. A significant saving in both storage and computation time (a factor of 50) was observed using this technique.

The predicted TL statistics are compared with actual TL observations from the ASIAEX 2001 East China Sea experiment. In general, about 80% of the observed TL data falls within 90% of the range-varying predicted TL probability distribution. Thus, the geoacoustic inversion has captured most of the uncertainty in the environment.

ACKNOWLEDGMENTS

This work was supported by the Office of Naval Research under Grant No. N00014-05-1-0264.

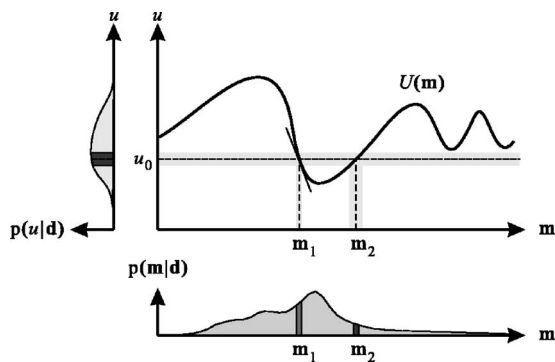


FIG. 11. Model-utility relationship: many-to-one transformations. In the center panel, horizontal axis represents the model domain, vertical axis represents the utility domain. The bottom and left panels indicate $p(\mathbf{m}|\mathbf{d})$ and $p(u|\mathbf{d})$, respectively.

APPENDIX: TRANSFORMATION OF RANDOM VARIABLES

Given that $u=U(\mathbf{m})$ and assuming that $U(\mathbf{m})$ is a monotonic function of \mathbf{m} (monotonic assumption only true in this paragraph), the posterior pdf of \mathbf{m} is related to the posterior pdf of u by the transformation of random variables

$$p(u|\mathbf{d}) = p(\mathbf{m}|\mathbf{d}) \left| \frac{\partial \mathbf{m}}{\partial U(\mathbf{m})} \right|, \quad (\text{A1})$$

where $|\partial \mathbf{m} / \partial U(\mathbf{m})|$ is the absolute value of the Jacobian determinant, whose reciprocal represents the hypervolume in the \mathcal{U} domain mapped out by the small hypercube region in the \mathcal{M} domain.

Propagation of parameter uncertainties to the TL predictions by integration in the sense of Eq. (16) can be related to the transformation of random variables as in Eq. (A1) using the properties of the Dirac delta function. Suppose that $f(x)=0$ has N zeros $\{x_n\}$ and $df(x_n)/dx \neq 0$, then $\delta(f(x))$ equals a sequence of impulses at $x=x_n$ of area $|df(x_n)/dx|^{-1}$,³⁷ i.e.,

$$\delta(f(x)) = \sum_n \delta(x-x_n) \left| \frac{df(x_n)}{dx} \right|^{-1}. \quad (\text{A2})$$

Using Eq. (A2), Eq. (16) can be rewritten as

$$p(u|\mathbf{d}) = \int_{\mathcal{M}} \delta[U(\mathbf{m}) - u] p(\mathbf{m}|\mathbf{d}) d\mathbf{m} = \sum_{n=1}^N p(\mathbf{m}_n|\mathbf{d}) \times \left| \frac{\partial U(\mathbf{m}_n)}{\partial \mathbf{m}} \right|^{-1}, \quad (\text{A3})$$

where $\{\mathbf{m}_n\}$ are the roots of the equation $U(\mathbf{m}) - u = 0$. Equa-

tion (16) is the generalization of Eq. (A1) to many-to-one transformations.

Equation (A3) can be explained intuitively using Fig. 11. For a nonmonotonic function $U(\mathbf{m})$, the probability mass of any specific value u_0 can be found by first solving for the roots of the equation $u_0 = U(\mathbf{m})$, then calculating the inverse of $|\partial U(\mathbf{m})/\partial \mathbf{m}|$ at the roots \mathbf{m}_n , weighted according to $p(\mathbf{m}_n|\mathbf{d})$, and finally summing all probability masses.

¹P. Gerstoft, "Inversion of seismoacoustic data using genetic algorithms and a *a posteriori* probability distributions," J. Acoust. Soc. Am. **95**, 770–782 (1994).
²P. Gerstoft and C. F. Mecklenbräuker, "Ocean acoustic inversion with estimation of a *a posteriori* probability distributions," J. Acoust. Soc. Am. **104**, 808–819 (1998).
³M. I. Taroudakis and M. G. Markaki, "Bottom geoacoustic inversion by broadband matched field processing," J. Comput. Acoust. **16**, 167–183 (1998).
⁴L. Jaschke and N. R. Chapman, "Matched field inversion of broadband data using the freeze bath method," J. Acoust. Soc. Am. **106**, 1838–1851 (1999).
⁵G. R. Potty, J. H. Miller, J. F. Lynch, and K. Smith, "Tomographic inversion for sediment parameters in shallow water," J. Acoust. Soc. Am. **108**, 973–986 (2000).
⁶D. P. Knobles, R. A. Koch, L. A. Thompson, K. C. Focke, and P. E. Eisman, "Broadband sound propagation in shallow water and geoacoustic inversion," J. Acoust. Soc. Am. **113**, 205–222 (2003).
⁷S. E. Dosso, "Quantifying uncertainty in geoacoustic inversion I: A fast Gibbs sampler approach," J. Acoust. Soc. Am. **111**, 129–142 (2002).
⁸F. B. Jensen and N. Pace, *Impact of Littoral Environmental Variability on Acoustic Predictions and Sonar Performance* (Kluwer Academic, The Netherlands, 2002).
⁹P. Abbot and I. Dyer, "Sonar performance predictions based on environmental variability," in *Impact of Littoral Environmental Variability on Acoustic Predictions and Sonar Performance*, edited by N. G. Pace and F. B. Jensen (Kluwer Academic, The Netherlands, 2002), pp. 611–618.
¹⁰K. R. James and D. R. Dowling, "A probability density function method for acoustic field uncertainty analysis," J. Acoust. Soc. Am. **118**, 2802–2810 (2005).
¹¹S. Finette, "Embedding uncertainty into ocean acoustic propagation models (I)," J. Acoust. Soc. Am. **117**, 997–1000 (2005).
¹²D. Tielburger, S. Finette, and S. Wolf, "Acoustic propagation through an internal wave field in a shallow water waveguide," J. Acoust. Soc. Am. **101**, 789–808 (1997).
¹³D. Rouseff and T. E. Ewart, "Effect of random sea surface and bottom roughness on propagation in shallow water," J. Acoust. Soc. Am. **98**, 3397–3404 (1995).
¹⁴P. Gerstoft, C.-F. Huang, and W. S. Hodgkiss, "Estimation of transmission loss in the presence of geoacoustic inversion uncertainty," IEEE J. Ocean. Eng. **31**, April issue, 2006.
¹⁵A. Tarantola, *Inverse Problem Theory and Methods for Model Parameter Estimation* (SIAM, Philadelphia, 2005).
¹⁶K. Mosegaard and A. Tarantola, "Probabilistic approach to inverse problems," in *International Handbook of Earthquake & Engineering Seismology, Part A* (Academic, London, 2002), pp. 237–265.
¹⁷L. T. Rogers, M. Jablecki, and P. Gerstoft, "Posterior distributions of a

statistic of propagation loss inferred from radar sea clutter," Radar Science **40**, 1–14 (2005).
¹⁸C. F. Mecklenbräuker and P. Gerstoft, "Objective functions for ocean acoustic inversion derived by likelihood methods," J. Comput. Acoust. **8**, 259–270 (2000).
¹⁹F. B. Jensen and M. C. Ferla, "SNAP: The SACLANTCEN normal-mode acoustic propagation model," SACLANT Undersea Research Centre, SM-121, La Spezia, Italy (1979).
²⁰C.-F. Huang, P. Gerstoft, and W. S. Hodgkiss, "Uncertainty analysis in matched-field geoacoustic inversions," J. Acoust. Soc. Am. **119**, 197–207 (2006).
²¹R. N. Bracewell, *The Fourier Transform and its Applications*, 3rd ed. (McGraw-Hill, New York, 2000).
²²W. H. Press, B. P. Flannery, S. A. Teukolsky, and W. T. Vetterling, *Numerical Recipes in Fortran 77*, 2nd ed. (Cambridge University Press, London, 1992).
²³N. Metropolis, A. W. Rosenbluth, M. N. Rosenbluth, A. H. Teller, and E. Teller, "Equation of state calculations by fast computing machines," J. Chem. Phys. **21**, 1087–1092 (1953).
²⁴S. Geman and D. Geman, "Stochastic relaxation, Gibbs distributions, and the Bayesian restoration of images," IEEE Trans. Pattern Anal. Mach. Intell. **6**, 721–741 (1984).
²⁵M. K. Sen and P. L. Stoffa, "Bayesian inference, Gibbs' sampler and uncertainty estimation in geophysical inversion," Geophys. Prospect. **44**, 313–350 (1996).
²⁶Z.-H. Michalopoulou and M. Picarelli, "Gibbs sampling for time-delay and amplitude estimation in underwater acoustics," J. Acoust. Soc. Am. **117**, 799–808 (2005).
²⁷D. Battle, P. Gerstoft, W. S. Hodgkiss, W. A. Kuperman, and P. Nielsen, "Bayesian model selection applied to self-noise geoacoustic inversion," J. Acoust. Soc. Am. **116**, 2043–2056 (2004).
²⁸C. Yardim, P. Gerstoft, and W. S. Hodgkiss, "Estimation of radio refractivity from radar clutter using Bayesian Monte Carlo analysis," IEEE Trans. Antennas Propag. **54**, 1318–1327 (2006).
²⁹M. D. Collins and L. Fishman, "Efficient navigation of parameter landscapes," J. Acoust. Soc. Am. **98**, 1637–1644 (1995).
³⁰G. L. D'Spain, J. J. Murray, W. S. Hodgkiss, N. O. Booth, and P. W. Schey, "Mirages in shallow water matched field processing," J. Acoust. Soc. Am. **105**, 3245–3265 (1999).
³¹W. R. Gilks, S. Richardson, and D. J. Spiegelhalter, *Markov Chain Monte Carlo in Practice* (Chapman and Hall, London, 1996).
³²C. J. Geyer, "Practical Markov chain Monte Carlo (with discussion)," Stat. Sci. **7**, 473–483 (1992).
³³C. P. Robert and G. Casella, *Monte Carlo Statistical Methods* (Springer-Verlag, New York, 1999).
³⁴P. Gerstoft, SAGA Users guide 5.0, an inversion software package, An updated version of "SAGA Users guide 2.0, an inversion software package," SACLANT Undersea Research Centre, SM-333, La Spezia, Italy (1997).
³⁵C.-F. Huang and W. S. Hodgkiss, "Matched field geoacoustic inversion of low frequency source tow data from the ASIAEX East China Sea experiment," IEEE J. Ocean. Eng. **29**, 952–963 (2004).
³⁶C.-F. Huang, P. Gerstoft, and W. S. Hodgkiss, "Data error covariance matrix for vertical array data in an ocean waveguide," J. Acoust. Soc. Am. **119**, 3272 (2006).
³⁷A. Papoulis, *Systems and Transforms with Applications in Optics* (McGraw-Hill, New York, 1968).